Stochastic image reconstruction for a dual-particle imaging system

M.C. Hamel[a*], J.K. Polack[a], A. Poitrasson-Rivière[a], M. Flaska[a], S.D. Clarke[a], S.A. Pozzi[a], A. Tomanin[b], P. Peerani[c]

[a] Department of Nuclear Engineering and Radiological Sciences, University of Michigan, 2355 Bonisteel Blvd, Ann Arbor, Michigan 48109, USA

[b] Lainsa-Italia S.R.L., via E. Fermi 2749, 21027 Ispra (VA), Italy

[c] European Commission, Joint Research Centre, Institute for Transuranium Elements, 21027 Ispra (VA), Italy

Email: mchamel@umich.edu, kpolack@umich.edu, alexispr@umich.edu, mflaska@umich.edu, clarkesd@umich.edu, pozzisa@umich.edu, alice.tomanin@jrc.ec.europa.eu, paolo.peerani@jrc.ec.europa.eu

Phone Number: 248.882.0790

*Corresponding Author

Abstract:

Stochastic image reconstruction has been applied to a dual-particle imaging system being designed for nuclear safeguards applications. The dual-particle imager (DPI) is a combined Compton-scatter and neutron-scatter camera capable of producing separate neutron and photon images. The stochastic origin ensembles (SOE) method was investigated as an imaging method for the DPI because only a minimal estimation of system response is required to produce images with quality that is comparable to common maximum-likelihood methods. This work contains neutron and photon SOE image reconstructions for a ^{252}Cf point source, two mixed-oxide (MOX) fuel canisters representing point sources, and the MOX fuel canisters representing a distributed source. Simulation of the DPI using MCNPX-PoliMi is validated by comparison of simulated and measured results. Because image quality is dependent on the number of counts and iterations used, the relationship between these quantities is investigated for many trials.

Keywords: Radiation Imaging; Image Reconstruction; Compton imaging; Neutron imaging; Radiation detection

1. Introduction

The principles of Compton-scatter photon imaging are well understood and have been applied to applications such as nuclear security and astrophysics. Compton-scatter cameras traditionally generate images by applying the Compton-scatter equation,

$$\cos\theta = 1 - \frac{m_e c^2 E_{d1}}{E_{d2}(E_{d1} + E_{d2})}$$

to calculate the angle, θ, from the scatter axis at which the photon originated. E_{d1} is the energy deposited by the photon in a scatter and E_{d2} is the energy remaining after the scatter. Each angle defines the surface of a cone that represents all possible origins of that event. To measure the required parameters for Eqn. 1, a Compton camera typically consists of a scattering and absorbing medium. This may consist of separate detector arrays or can be accomplished with position sensitive detectors. Recorded counts are *correlated events* which correlate the two required interactions to calculate the scatter angle. A neutron-scatter camera defines cones in a similar fashion to the Compton camera but instead uses elastic scattering events in two different detectors [1], [2]. The cones are projected onto a surface and their superposition produces an image of the source. This method, often referred to as simple backprojection, produces images with a large point-spread function partly due to the inclusion of the entire cone in the image. The image is also blurred because effects inherent to radiation measurements, and the construction of the imaging system, cause many cones to not overlap with the actual source location. These effects include detector energy and timing resolution as well as positional uncertainty of the particle interaction within an individual detector.

Statistical techniques for image reconstruction have improved image quality for Compton-scatter and neutron-scatter cameras compared to simple backprojection. One such method, maximum-likelihood expectation-maximization (MLEM) has been widely implemented [3]–[6]. Another technique, stochastic origin ensembles (SOE) has been proposed as an alternative to MLEM. It was shown that SOE image reconstruction provides comparable image quality to MLEM by Andreyev et al., and does so without requiring an extensive estimate of input parameters to describe system response [7]. The only inputs required for SOE image reconstruction are the backprojected cones and a single value describing the angular resolution of the system. This is significant because deriving or simulating system response is often computationally intensive. For a system that uses multiple detector configurations, depending on the application, creating a large number of system response functions may not be feasible.

SOE has been applied to tomographic reconstruction as well as adapted to Compton-scatter cameras for medical imaging applications [8]–[10]. These studies presented the method for SOE image reconstruction and showed simulated results from Compton cameras meant for close-range imaging. However, in safeguards, large fixtures such as containers and pipes must be measured, which requires a longer source-to-detector distance than is typical in medical applications. Consequently, safeguards applications require a larger system to obtain reasonable detection efficiency.

Imaging both photons and neutrons is of great interest in these applications as it may provide a more robust detection of shielded SNM, that emits both neutrons and photons, when intervening material is present. A typical source for a safeguards measurement will provide a high photon count rate compared to the neutron count rate – typically by an order of magnitude or more [11]. However, photon background radiation will have a significant effect on image reconstruction. Safeguard measurements are typically performed in facilities containing other radioactive sources contributing a high rate of photon background radiation [11]. In comparison, neutron background rates are generally lower.

This paper investigates the application of SOE imaging to a dual-particle imaging system for safeguards applications at standoff distances of several meters. The dual-particle imaging system combines a traditional Compton-scatter camera with a neutron-scatter camera in a two-plane design [12], [13]. We have chosen to investigate the feasibility of SOE image reconstruction because only a minimal definition of system response is required to produce images that may offer quality comparable to MLEM solutions.

2. Image-reconstruction method

The SOE algorithm for this study was implemented as a modified version of the method proposed by Andreyev et al. [7]. SOE reconstruction uses the Metropolis-Hastings algorithm which relies on Markov-Chain Monte Carlo sampling to produce an image. A full derivation of the SOE method is presented by Sitek for use in tomography [8]. A brief description of the method implemented in this study follows.

1) Let $\boldsymbol{N}$ represent the total number of events. A cone for each event is projected onto a pixelated sphere that is centered in between the front and back plane of the DPI and extends beyond the system. The intersection of the cone and sphere defines a region of possible source origins that is close in shape to a circle. Each projected cone is broadened by 8° both inside and outside of the intersection. This broadening accounts for resolution effects that shift projected cones away from the actual source location.

The size chosen for the broadening of the projected cones is described in detail in section 2.2.

2) The location for a single origin, $\boldsymbol{k}$, is randomly sampled as a pixel from each projected cone. The collection of origins is the starting image state $\boldsymbol{Y_0}$.

3) A new, potential image state, $\boldsymbol{Y_{s+1}}$, is created by randomly selecting a single origin, $\boldsymbol{k}$, from $\boldsymbol{Y_s}$, for a possible move to a new pixel. The new pixel is randomly sampled from those within the broadened projection of the cone. The number of origins located at the new pixel, in state $\boldsymbol{s+1}$ ($\boldsymbol{P_{k,s+1}}$), is compared to the number of origins located at the old pixel, in state $\boldsymbol{s}$ ($\boldsymbol{P_{k,s}}$).

4) The new location of $\boldsymbol{k}$ will be accepted or rejected based on an acceptance probability defined as

$$A(Y_s \rightarrow Y_{s+1}) = \min\left(1, \frac{P_{k,s+1}+1}{P_{k,s}}\right).$$

If the new location of $\boldsymbol{k}$ is accepted, the current image state becomes $\boldsymbol{Y_{s+1}}$, otherwise the current image state remains as $\boldsymbol{Y_s}$. Based on the acceptance probability $\boldsymbol{A}$, if an origin is moved to a pixel with more origins, the current image state will be accepted. The addition of one to $\boldsymbol{P_{k,s+1}}$, in Eqn. 2, represents the possible movement of origin $\boldsymbol{k}$. If the number of pixels at the new location is lower, the acceptance probability is the ratio of the number of pixels at the new location to the number of pixels at the old location. The acceptance probability is designed such that origins are preferentially moved to pixels with more origins, which represent a higher probability of being the source location.

5) A single iteration of the algorithm is defined as the repetition of steps (3) and (4) N times. The algorithm is then performed for a number of iterations until the image reaches a quasi-stationary state. An investigation of the required number of iterations is presented in section 3.2.

The main difference between our implementation of SOE and the method proposed by Andreyev et al. is the representation of space from which each origin is sampled. Because the DPI was optimized for sources at standoff distances, three-dimensional imaging is not feasible. For this reason, our implementation of SOE sampled each origin from the circular projection of each cone onto a sphere. Two methods for the projection of cones onto a sphere are used for different applications. For far-field imaging, the apex of each cone is located at the system center. The system center is defined as the middle point of the gap between the front and back planes. In this case, the radius of the sphere is irrelevant because any radius will provide the same result. For near-field imaging, the apex of each cone is centered in the front-plane detector that recorded the initial scattering event. An approximate distance to the source must be known, and used for the sphere radius.

2.1 Resolution recovery

To achieve better convergence of the event origins, we used a modified version of a method proposed by Andreyev et al. for resolution recovery [14]. Each projected cone was broadened by a fixed amount to account for the effects of energy, time, and spatial uncertainty. A study was conducted to determine the optimum broadening for projected cones using measured and simulated results.

2.1.1 Measurement and simulation of DPI resolution

Figure 1 shows the DPI constructed as follows: A front plane consisted of a 4×4-square grid of EJ-309 liquid scintillators that were 5.1 cm thick and had a diameter of 7.6 cm with detectors spaced at 15 cm intervals (measured from detector centers). A back plane contained EJ-309 liquid scintillators and NaI(Tl) scintillators in a 4×4-checkerboard pattern. Both types of back-plane detectors had a thickness of 7.6 cm and a diameter of 7.6 cm and were spaced at 25 cm intervals. The planes were separated by 30 cm [12], [15].

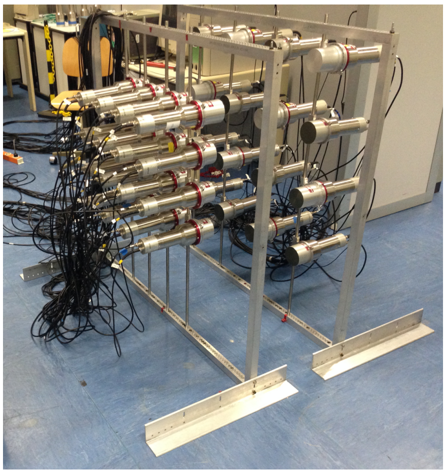

Figure 1: The DPI is a two plane Compton scatter and neutron scatter camera.

The DPI was simulated with the Monte Carlo code MCNPX-PoliMi and post-processor MPPost [16], [17]. To accurately model the full system resolution, which defines the accuracy of recorded counts, it was imperative that the energy resolution and neutron light output response for the EJ-309 liquid scintillators was well characterized. The functions used in these simulations were found empirically by Enqvist et al. [18]. The exponential fit for the neutron light output function found by Enqvist et al. for the 7.6 cm thick × 7.6 cm diameter EJ-309 liquid scintillator was used for all liquid scintillators in our model:

$$Light\ Output = 0.817\,E - 2.63\,(1 - e^{-0.297\,E}).$$

In Eqn. 3, *Light Output* is in units of MeVee and *E* represents the energy of the recoil proton in MeV. Current capabilities of MPPost do not allow for the input of multiple light output coefficients and using the fit for the 7.6 cm thick × 7.6 cm diameter detectors was found to give better agreement with measurements than the fit found for the 5.1 cm thick × 5.1 cm diameter detectors. The resolution function used for all liquid scintillators in the model was

$$\left(\frac{\Delta E}{E}\right) = \sqrt{0.113^2 + \frac{0.065^2}{E} + \left(\frac{0.060}{E}\right)^2}.$$

The coefficients found for this equation by Enqvist et al. were only given for the 7.6 cm thick × 7.6 cm diameter detectors in the DPI so these coefficients were also applied to the 5.1 cm thick × 5.1 cm diameter detectors. The energy resolution used for the NaI(Tl) scintillators was given by Roemer et al. [19] as

$$\frac{fwhm}{E} = \left(811 \times E^{-1.06} - 5 \times \left(\frac{E}{4000}\right)^{1.8} + 6.2\right)\%.$$

Timing resolution of the detectors was also included in the simulations. Gaussian sampling with empirically found FWHM values for each detector type was applied to the arrival time of each event in the simulation. A FWHM of 1 ns was used for the EJ-309 liquid scintillators and a FWHM of 10 ns was used for the NaI(Tl) scintillators. For both measurement and simulation, energy thresholds of 80 keVee were used for the liquid scintillators and 32 keVee for the NaI(Tl) scintillators. The dynamic range of the waveform digitizer use for data acquisition limited the maximum light output to 3.180 MeVee for a single pulse.

Non-active detector materials such as photomultiplier tubes, detector casing, and optical windows were also included in the simulations. Counts recorded in the simulations were categorized as either *ideal counts* or *non-ideal counts*. Examples of non-ideal counts included: events that scattered in active and non-active detector material, events that underwent multiple scatters in a single detector or the correlation of two different particles. Another type of non-ideal count is caused by an incorrect ordering of interaction locations due to time resolution. Viewing both types of counts in the simulation provided the information to optimize the allowed range of origin movements. The goal was to minimize the range of distances that each origin from an ideal count could move while still allowing it to reach the source location.

A ^{252}Cf source emitting approximately 165,000 neutrons per second was measured to provide a comparison with simulated results. The source was located 271 cm from the center of the DPI (inclination: 90°, azimuth: 90°). The fission neutrons and photons from the ^{252}Cf source were simulated for the same source location using the source energy distributions for Cf-252 from MCNPX-PoliMi for both particles [16]. For each correlated event, the minimum angular distance from the source location to the projected cone was calculated in degrees using spherical coordinates. Near-field imaging was used for cone projection onto a sphere with a radius of 271 cm. The minimum angular distances were histogrammed for measurements and simulations to create resolution distributions. Cumulative distributions were also computed to evaluate the total fraction of counts that were included for a specific range of angular distances.

2.2 DPI resolution results

Figure 2 shows a comparison between the measured and simulated neutron resolution distributions. The measured and simulated distributions both showed a large drop in counts between 8° and 10°. The simulated distribution had a higher fraction of counts with smaller minimum angular distances than the measurement. This is because more non-ideal counts were measured than were simulated due to scattering off of materials in the laboratory not included in the simulation. Those materials included the rack holding the detectors and concrete walls. Simulated distributions for ideal and non-ideal counts in Figure 3 showed that 96% of ideal counts were contained in the 0° to 8° range. The non-ideal counts composed a greater fraction of the large minimum angular distances than ideal counts, with the distribution decreasing in a linear fashion.

The range chosen for the broadening of a projected neutron cone was 8° because almost all ideal counts were located within this distance from the projected cones. The 8° broadening maximized the probability that the true source location was sampled and minimized the amount of possible locations for sampling. For the measured ^{252}Cf source, Figure 2 shows that the 8° range allowed for 58% of total neutron counts to be sampled at the correct source location.

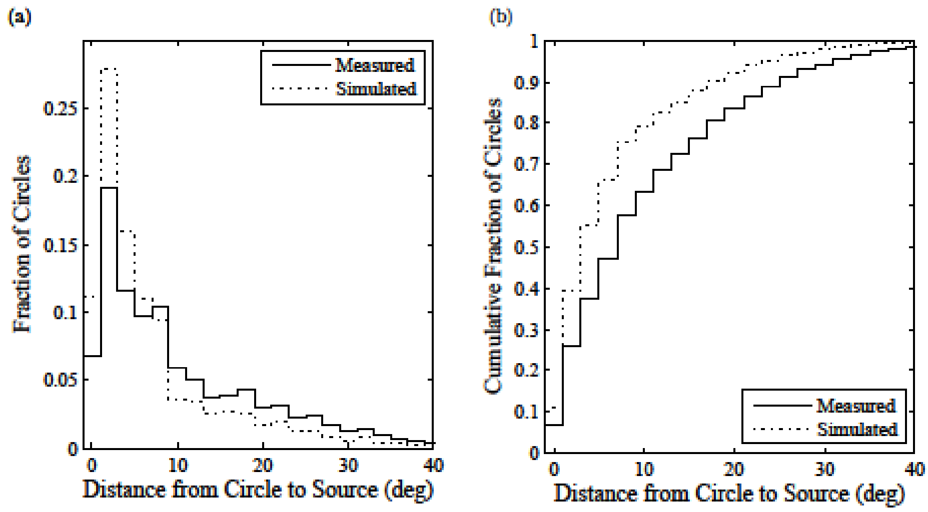

Figure 2: Measured and simulated probability distributions (a) and cumulative distributions (b) for total neutron counts. The measured cumulative distribution showed that 58% of events were within 8° of the source location.

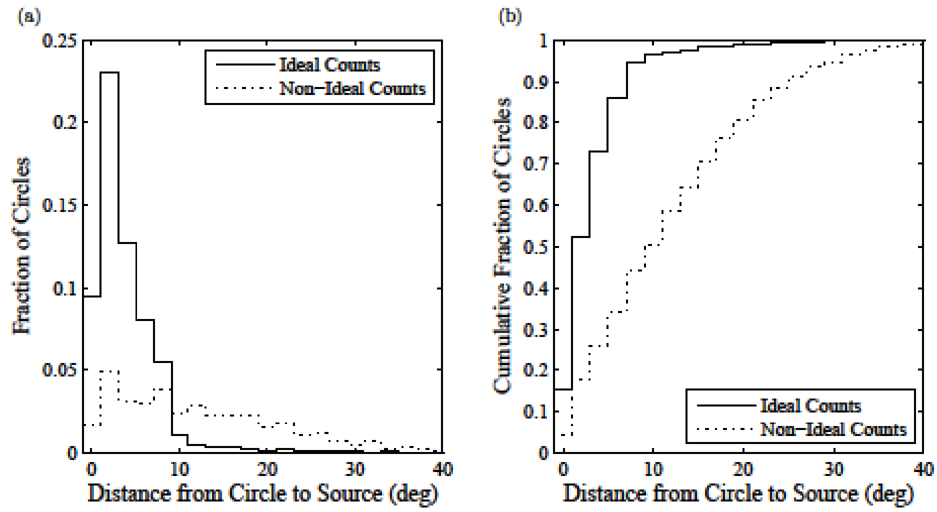

Figure 3: Simulated probability distributions (a) and cumulative distributions (b) for ideal and non-ideal neutron counts.

The same technique was used for the analysis of correlated photon events. The distribution of measured photon events, compared with the simulated distribution in Figure 4, did not agree as well with the simulation as the neutron distributions. This disagreement was due to a high contribution from photon background radiation. For this case, the simulation, which did not contain a contribution from background radiation, had to be used to find the appropriate angular distance from which a pixel can be sampled from a cone. Figure 5 shows that the fraction of ideal photon counts decreased significantly after 8°. Because the non-ideal counts showed a decreasing linear trend and a much lower contribution than ideal counts, the broadening of projected photon cones was also chosen to be 8°. This range allowed only 16% of measured, total photon counts, shown in the cumulative distribution in Figure 4, to reconstruct to the correct source location.

The fraction of photon counts that were within 8° of the source location was significantly less than for neutrons counts. However, photon counts that were not overlapped with the true source location were more likely to have been created from background radiation or non-ideal counts, which would be more evenly distributed over the imaging space than ideal counts. Despite the contribution of background radiation and non-ideal counts, a visible hot-spot was still produced when imaged.

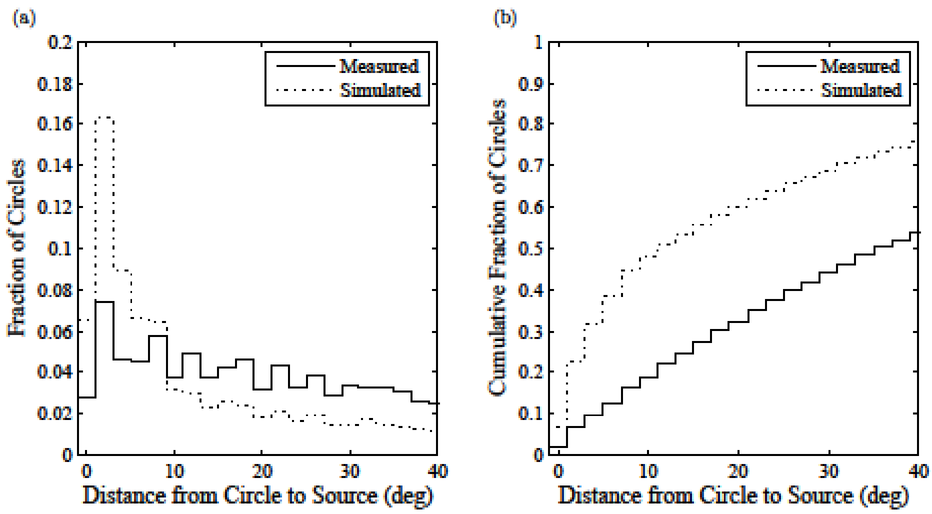

Figure 4: Measured and simulated probability distributions (a) and cumulative distributions (b) for total photon counts.

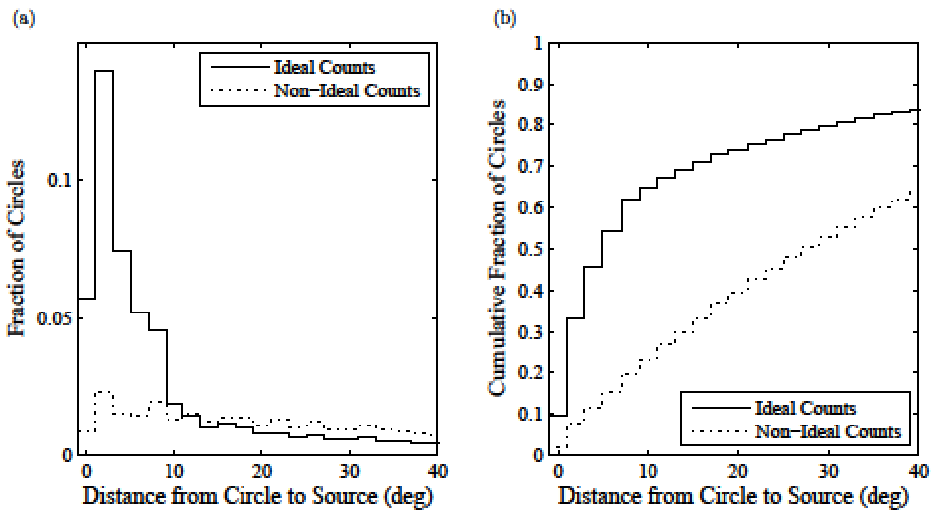

Figure 5: Simulated probability distributions (a) and cumulative distributions (b) for ideal and non-ideal photon counts.

3. Measurement and simulation results and discussion

Both measurement and simulation results were used to demonstrate the effectiveness of SOE image reconstruction. These results were also used to evaluate parameters such as number of counts and number of iterations required to reach a quasi-stationary image state.

3.1 Comparison of SOE to MLEM

A comparison between the image quality of SOE and MLEM solutions was made. The MLEM method used relies on a simulated system response-matrix using the parameters described in section 2.1.1. A full explanation of the MLEM algorithm developed for the DPI can be found in [20].

A ^{252}Cf and ^{60}Co source were measured simultaneously to compare both neutron and photon performance of both imaging methods [21]. The ^{252}Cf emitted 124,000 neutrons per second and was located 175 cm from the center of the system at (114° azimuth, 93° inclination). The ^{60}Co had an activity of 63 μCi and was located 390 cm from the center of the system at (58°, 84°). The measurement time was 350 minutes.

The SOE and MLEM images were created using 5° pixels. For SOE, the neutron image used near-field imaging with cones projected on a sphere with a radius of 175 cm. The photon image used the far-field approximation which provided better results because the sources were located at different distances. The SOE neutron image in Figure 6 (a) shows the correct location of the ^{252}Cf source. The SOE photon image in Figure 6 (b) shows two hot-spots, a more intense hot-spot in the location of the ^{60}Co and a less intense hot-spot where the ^{252}Cf is located. The MLEM neutron and photon images, in Figure 7, also show hot-spots in the correct locations for both sources. The SOE and MLEM images provide comparable images that offer better signal-to-noise ratio and resolution than simple backprojection. Figure 8 shows the simple backprojection images for both neutrons and photons. The hot-spots created by simple backprojection are much larger and the signal-to-noise ratio suffers from artifacts caused by inclusion of the entire cone projection on the image.

To evaluate the quality of the SOE images, the percentage of total measured counts contained in the 3 × 3 pixel regions centered at (115°, 95°) and (60°, 85°) were compared to the same percentages for the MLEM images in Table 1. The SOE neutron image constructs 12.4% more counts than the MLEM solution to the same region. While SOE reconstructs a higher percentage of counts to the region, there is more noise present toward the center of the image compared to the MLEM solution.

In the photon solution the percentages comparing both hot-spots agree better with the SOE, constructing 1.4% more counts for the ^{252}Cf hot-spot and 1.7% more counts for the ^{60}Co hot-spot than the MLEM solution. Again, there is more noise present in between the two sources in the SOE solution, although more counts reconstructed to the hot-spots. The noise on the edges of the MLEM photon image was likely due to background radiation counts coming from behind the system. The system matrix for the MLEM solution only consists of the two-pi hemisphere in front of the system. As such, the most likely location for these counts to reconstruct in a two-pi hemisphere is along the azimuthal edges.

It may be possible to remove some of the noise seen in the SOE images that is not present in the MLEM images by averaging each image state after completing a certain number of iterations. This averaging method is used by Sitek in tomographic image reconstruction [8]. However, if the images are not averaged, each individual pixel will contain a collection of counts that are tagged with energy. This allows an individual energy spectrum to be viewed for each pixel, which can help identify sources if more than one is present. This work does not use averaging, which maintains an energy spectrum for each pixel that has not been averaged.

In general, the hot-spots for the MLEM solutions appear as broader peaks than the SOE solutions. Further implementation of an averaging method for SOE may broaden the hot-spots. Broadening may be advantageous in a case such as the ^{60}Co hot-spot in which the hot-spot appears as two intense pixels located adjacently along a diagonal when only one source is present in that region.

Table 1: The percentage of counts contained within a 3 × 3 pixel region of each source for neutrons and photons.

^{252}Cf Neutrons		^{252}Cf Photons		^{60}Co Photons	
SOE	MLEM	SOE	MLEM	SOE	MLEM
35.6%	23.2%	3.8%	2.4%	7.1%	5.4%

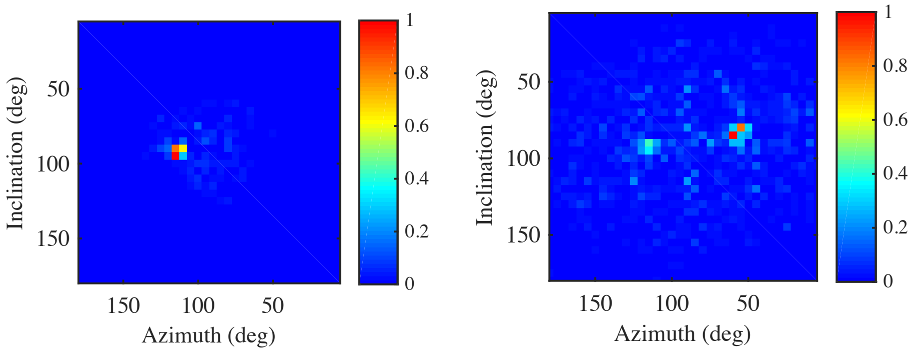

Figure 6: Reconstructed SOE images for neutrons (a) and photons (b). The neutron hot-spot correctly locates the ^{252}Cf source. The photon image shows two hot-spots, with the more intense spot locating ^{60}Co and the less intense hot-spot locating the ^{252}Cf.

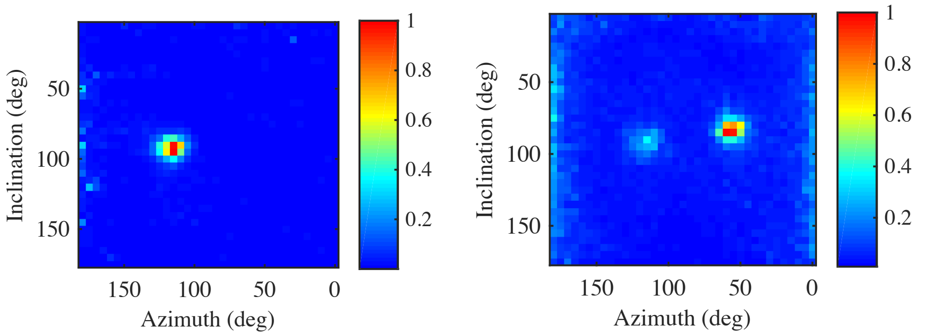

Figure 7: Reconstructed MLEM images for neutrons (a) and photons (b). The neutron image shows a single hot-spot locating the ^{252}Cf and the photon image shows two hot-spots locating the ^{252}Cf and the more intense ^{60}Co.

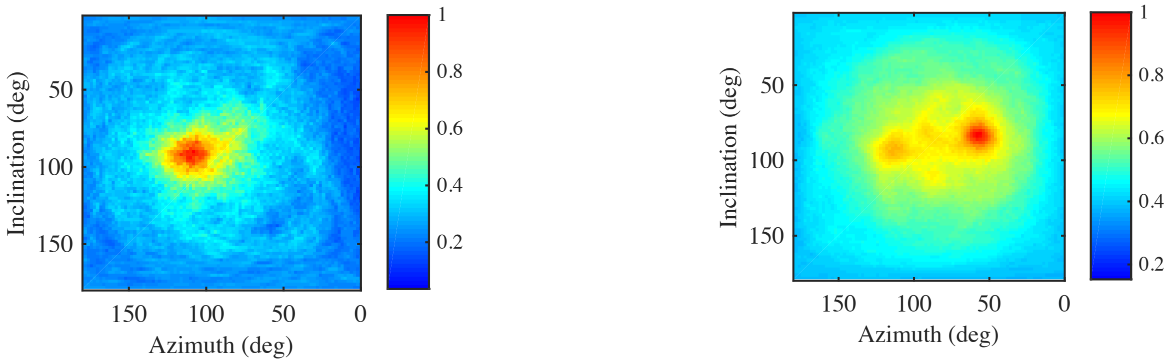

Figure 8: Simple backprojection neutron (a) and photon (b) images. The neutron image shows the single hot-spot from ^{252}Cf and the photon image shows multiple hot-spots from the ^{252}Cf and ^{60}Co.

3.2 Test cases

Three test cases were used in this analysis: a point source, two point sources, and a distributed source. The sources used were ^{252}Cf and mixed-oxide nuclear fuel (MOX) canisters. The ^{252}Cf emitted neutrons and photons through spontaneous fission (SF) as well as photons from radioactive decay. The MOX fuel emitted neutrons through spontaneous fission and (α,n) reactions and emitted photons through spontaneous fission and various radioactive decay chains. Each MOX fuel canister had a diameter of 13.5 cm and a height of 27 cm, and was contained in a steel canister. The images for the test cases were generated on a spherical mesh consisting of 8° pixels. The canisters represented point sources in this measurement due to the image pixel size and distance from the system. The isotopic composition of the MOX canisters is given in Table 2. ^{241}Pu, ^{234}U, and ^{236}U were also present in the MOX fuel in trace amounts. These isotopes did not significantly contribute to the neutron emission. Because of the high photon-to-neutron emission ratio of the MOX, both canisters were placed in by 8-mm lead sheaths. The shielding eliminated a large number of low energy photons, which originally resulted in count rates that were too high for the acquisition system to process.

The reconstructed images for each test case showed consistent reconstruction using 10,000 iterations of the SOE algorithm and a pixel size of 8°. The only exception was the measured photon image of the distributed source. A more thorough investigation of the number of iterations required to reach a quasi-stationary image state is presented in section 3.2. The larger 8°-pixels were used in this study because it provided better image reconstruction than 5° pixels.

Table 2: Approximate isotopic composition and neutron emission percentages for MOX canisters.

Isotope	Pct. of neutrons emitted	Approximate Weight Pct.
^{240}Pu	58% (SF)	4.6%
	8% (α,n)	

^{241}Am	17% (α,n)	0.5%
^{242}Pu	7% (SF)	0.3%
^{239}Pu	5% (α,n)	10.9%
^{238}Pu	1% (SF)	0.02%
	4% (α,n)	
^{238}U	~0%	66.8%
^{235}U	~0%	0.5%
O	N/A	16.1%

3.2.1. Single point source

A ^{252}Cf source emitting 165,000 neutrons per second was located 271 cm from the center of the system at an inclination of 90° and an azimuth of 90° (directly in front of the system). A 1,100-minute measurement was performed. The SOE algorithm, using near-field imaging with a sphere radius of 271 cm, reconstructed the point source to the correct location for the measured and simulated neutron images shown in Figure 9. Because the SOE method is stochastic, the number of counts reconstructed to the source pixel differed between two separate reconstructions. For this reason, the count rate values, for each source pixel, given in Table 3 are expressed as the average of multiple trials with the uncertainty given as one standard deviation. The images shown are an example of a single reconstruction.

For the neutron images in Figure 9, the average percentage of counts that reconstructed to the source pixel for the simulation was 43.7% compared to 24.3% for the measurement. As a result, the simulation created a sharper image than the measurement. The blurring seen in the measurement compared to the simulation is because more non-ideal counts, which may not reconstruct to the true source location, were present in the measurement than the simulation.

The simulation only included the concrete floor in the room so it is possible that other objects in the room and walls were the cause of additional non-ideal counts.

The measured photon image reconstructed the correct source location in Figure 10 (a). However, the average percentage of counts that reconstructed to the correct source pixel was 2.1%, which was much lower than for the neutron image. The smaller percentage of counts in the source pixel, compared to the neutron image, was due to a much higher count rate of background photons compared to background neutrons. The image clearly showed a lower signal-to-noise ratio than the neutron image but the source was still visible.

The simulated case in Figure 10 (b) shows the same hot-spot as the measured case. The source definition used for the simulation was from MCNPX-PoliMi and included only photons created from the spontaneous fission of Cf-252, the model did not include decay photons or background radiation. In comparison of the measured and simulated images, noise is present in the measured image that is not present in the simulated image. This strongly suggests that the noise in the measured image is created from environmental background radiation because no background was included in the simulation. Figure 11 shows an example of a photon background radiation image processed using the same parameters as the ^{252}Cf photon image. A similar pattern of noise is seen in this image compared to the ^{252}Cf photon image. However, the presence of a source lowers the relative intensity of non-source pixels in the image compared to the source-pixel.

Table 3: Image reconstruction results for measured and simulated ^{252}Cf point source. The reported error represents one standard deviation.

Neutrons	Photons

	Measured	Simulated	Measured
Total counts per second	0.138 ± 0.0014	0.121 ± 0.0014	11.6 ± 0.0056
Average counts per second in source pixel	0.0334 ± 0.0014	0.0527 ± 0.0015	0.0439 ± 0.0032
Average pct. of total counts in source pixel	24.3 ± 1.0	43.7 ± 1.3	2.1 ± 0.15

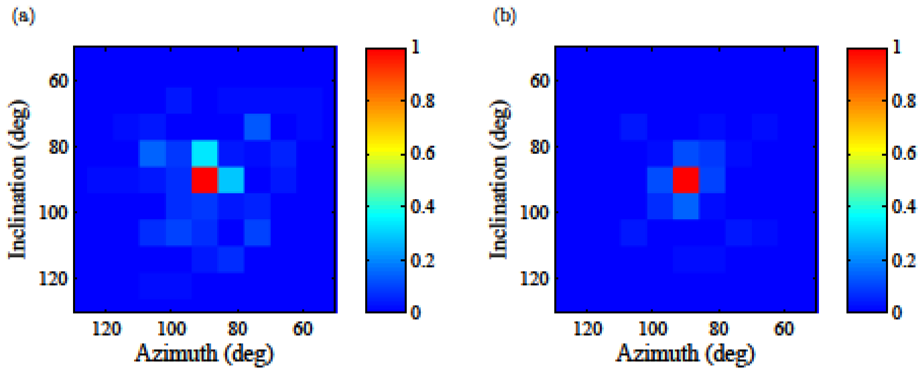

Figure 9: Reconstructed neutron images for a measured (a) and simulated (b) ^{252}Cf point source.

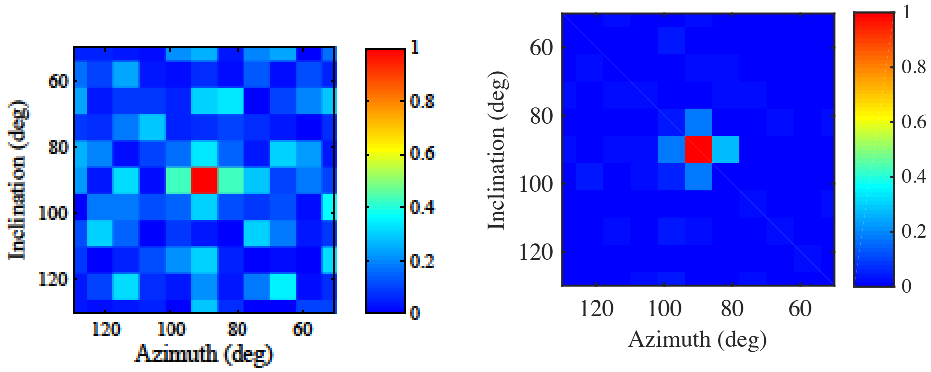

Figure 10: Reconstructed photon image for a measured ^{252}Cf point source.

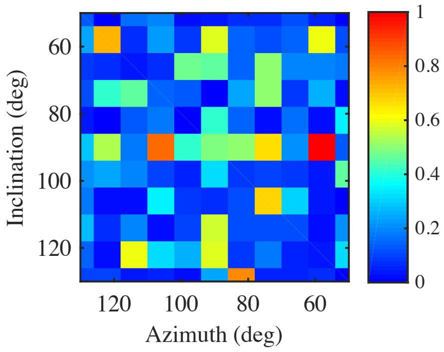

Figure 11: Reconstructed photon image of background radiation.

3.2.2. Two point sources

Both MOX canisters were arranged with their longer axis in a vertical orientation and the center of each canister located 250 cm from the center of the DPI. The canisters were separated by 25° horizontally; the corresponding coordinates were (77.5°, 90°) and (102.5°, 90°) with activities of 93,000 and 82,000 neutrons per second respectively. The setup is shown in Figure 12. A 120-minute measurement was performed. The mesh used for image reconstruction was shifted by 4 degrees along the azimuth compared to the previous point source case. This shift was made because, in the previous mesh, both sources were located on the edge of a pixel causing counts to appear in two pixels. Eliminating counts from one source appearing in two pixels allowed for better analysis of SOE image reconstruction. Near field imaging with a 250 cm sphere was used. Table 4 provides a summary of count rates averaged for multiple image reconstructions.

Two distinct hot-spots were reconstructed for both the measured and simulated images, shown in Figure 13, at the correct locations. The expectation was for the left source pixel to contain approximately 12% less counts than the right pixel due to the difference in neutron activity between the MOX canisters. However, the left source pixel contained 9% more counts on average than the right source pixel. A possible explanation is that the neutrons from the MOX fuel were not emitted isotropically and were biased either toward or anyway from the DPI. The source was a powder and likely had some form of heterogeneity present in its composition.

The photon reconstruction, in Figure 14, showed that both sources reconstructed to the correct pixels. The photon activity for the MOX samples was not available - because they were complex sources - so no conclusions could be drawn from the relative intensity of each pixel. Less noise appeared in the image than in the ^{252}Cf photon image in Figure 10. This observation suggested that the MOX fuel produced a larger source-to-background-radiation ratio than in the ^{252}Cf measurement, which was expected due to the high photon activity of plutonium. The average percentage of counts contained in the correct source pixel(s), 3.3% and 2.7% for the MOX fuel and 2.1% for the ^{252}Cf, supported the assumption that a smaller source-to-background-radiation ratio was the cause of noise in the ^{252}Cf photon image.

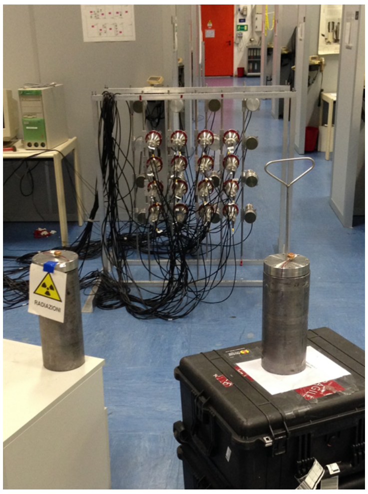

Figure 12: Measurement setup for two point sources.

Table 4: SOE Image reconstruction results for measured and simulated MOX canisters. The reported error represents one standard deviation.

	Neutrons		Photons
	Measured	Simulated	Measured
Total counts per second	0.204 ± 0.0053	0.195 ± 0.0052	28.5 ± 0.0629

Average counts per second in left source pixel	0.0357 ± 0.0046	0.0315 ± 0.0042	0.259 ± 0.0125
Average counts per second in right source pixel	0.0324 ± 0.0050	0.0364 ± 0.0043	0.214 ± 0.0144
Average pct. of total counts in left source pixel	17.5 ± 2.3	16.2 ± 2.2	3.3 ± 0.15
Average pct. of total counts in right source pixel	15.9 ± 2.5	18.6 ± 2.2	2.7 ± 0.18

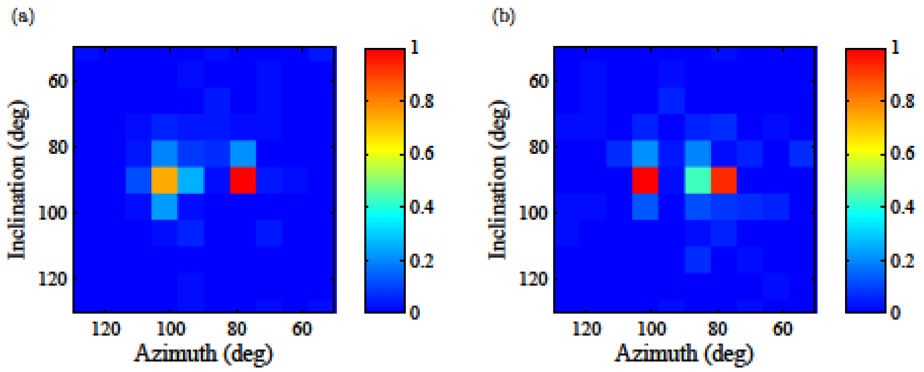

Figure 13: Reconstructed neutron image for a measurement (a) and simulation (b) of two MOX canisters separated by 25°.

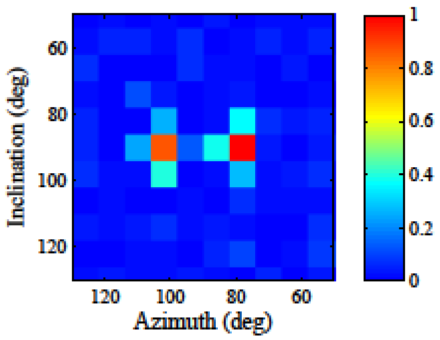

Figure 14: Reconstructed photon image for a measurement of two MOX canisters separated by 25°.

3.1.3. Distributed source

The two MOX canisters were used to represent a distributed source, as shown in Figure 15. The MOX canisters were placed in a horizontal line, with the center of the line located 148 cm from the center of the DPI. The center of the line had an angular location of (90°, 99.5°). The canisters subtended 23° along the azimuth and 5.2° in inclination. Five-centimeter thick lead bricks were placed in front of the canisters to increase the detected neutron-to-photon ratio. The mesh used for the image was aligned so that the height of each MOX canister, while lying on its side, was contained in a single pixel. The reconstructed images were made with near-field imaging using a sphere with a radius of 148 cm. The count rates for the image reconstructions are summarized in Table 5.

The neutron image reconstructions for both the measured and simulated cases showed the distributed source in the correct location. The image in Figure 16 (a) represents a good reconstruction as the source was clearly located in the correct pixels. Occasionally the reconstructed image showed less constant intensities across all three pixels. This observation was not as pronounced for the simulated image, which consistently showed a correct reconstruction. Because the measurement only contained 2,161 total counts, future measurements with distributed sources will focus on accumulating better statistics to achieve a consistent reconstruction with a distributed source. Another possible cause of the inconsistent reconstruction may have been the presence of the lead shielding. While lead is a relatively poor neutron moderator due to the low energy transfer to recoil nuclei, some neutrons that collided in the lead were scattered back into the path of the DPI and imaged. The reconstructed image contained both un-collided counts from the MOX and counts that had scattered in the lead.

The measured photon image, in Figure 17, showed a noisy reconstruction without an easily identifiable source. The lead shielding caused the source-to-background radiation rate to be too low for good reconstruction. The source pixels contained a very low percentage of total counts: approximately 1%. Both measurements previously discussed in this paper showed clear photon reconstruction and a larger percentage of the total counts (2.1% for ^{252}Cf and 3.3% and 2.7% for two MOX point sources) in the source pixels. The larger percentage of counts in a pixel corresponded to a larger signal-to-noise ratio. This relationship supported the conclusion that the source-to-background-radiation ratio is the cause of a noisy reconstruction for the photon image of the distributed source.

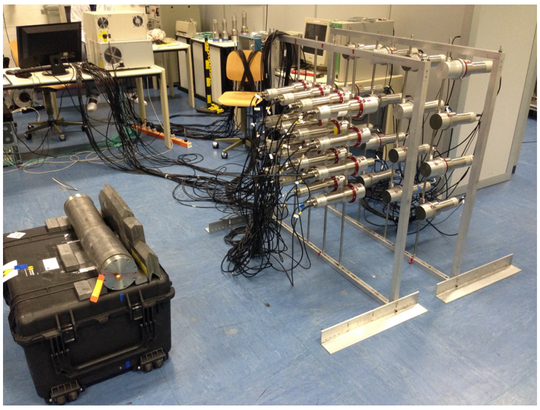

Figure 15: Measurement setup for a distributed source

Table 5: Image reconstruction results for measured and simulated MOX canisters. The given error represents one standard deviation.

	Neutrons		Photons
	Measured	Simulated	Measured
Total counts per second	0.400 ± 0.0086	0.434 ± 0.0089	14.9 ± 0.0525
Average counts per second in left source pixel	0.0544 ± 0.0075	0.0616 ± 0.0069	0.100 ± 0.0298
Average counts per second in center source pixel	0.0615 ± 0.0096	0.0580 ± 0.0092	0.167 ± 0.0295
Average counts per second in right source pixel	0.0296 ± 0.0075	0.0525 ± 0.088	0.131 ± 0.0204
Average pct. of total counts in left source pixel	13.6 ± 1.9	14.2 ± 1.6	0.67 ± 0.20
Average pct. of total counts in center source pixel	15.4 ± 2.4	13.4 ± 2.1	1.1 ± 0.20
Average pct. of total counts in right source pixel	7.4 ± 1.9	12.1 ± 2.0	0.88 ± 0.14

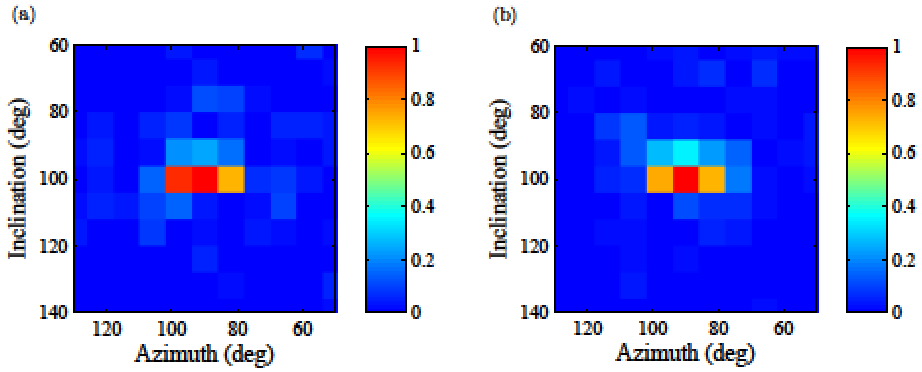

Figure 16: Reconstructed neutron image for a measurement (a) and simulation (b) of two MOX canisters laid end-to-end spanning 23°.

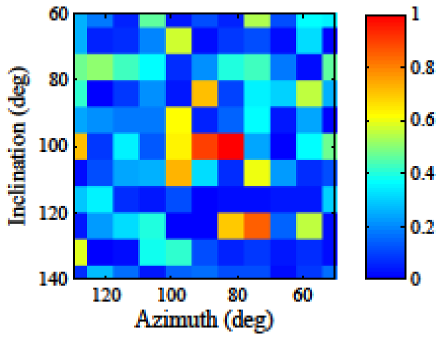

Figure 17: Reconstructed photon image for a measurement of two MOX canisters laid end-to-end spanning 23°.

3.3. Reconstruction parameters

Proper image reconstruction is dependent on enough counts and iterations being used to reach a quasi-stationary image state [7]. After this state is reached, more iterations will not improve or degrade image quality [7]. To evaluate what constitutes a sufficient number of counts and iterations, many combinations of these parameters were used to reconstruct an image for a single measurement. The number of counts that reconstructed to the correct pixel or pixels was summed over a number of trials. This result was then averaged and expressed as a percentage of total counts with the error expressed as one standard deviation. Neutron images were used for both cases to eliminate the contribution of background radiation on the analysis. Analysis was performed using the point source and two-point sources cases. The image reconstruction of the line source did not always produce the expected hot-spots in the three pixels containing the source. For this reason, it was not used in the evaluation of counts and iterations required to reach a quasi-stationary state.

3.3.1. Single point source

The results in Figure 18 shows the percentage of counts that reconstructed to the correct pixel. In general, as the total number of counts used for image reconstruction increased, a higher percentage of counts reconstructed to the correct source pixel. The results with uncertainty are given in Table 6. For the cases with at least 500 counts, image quality did not improve after 1,000 iterations. This analysis also showed that using 10,000 iterations of the SOE algorithm was appropriate to achieve a quasi-stationary image for a point source.

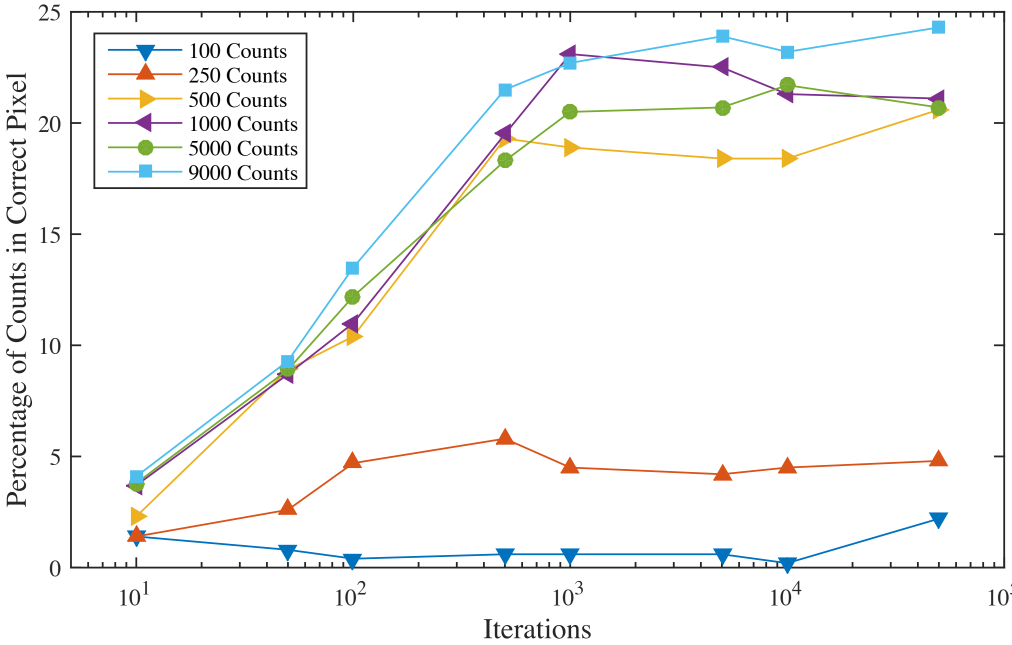

Figure 18: For a single point source, two parameters, total counts and number of iterations, were compared for differing numbers of counts. For cases with at least 500 counts, image quality did not improve after 1,000 counts.

Table 6: Percentage of neutron counts that reconstructed to the source pixel for different combinations of counts and iterations. The error is expressed as one standard deviation.

	Total Counts					
Iterations	**100**	**250**	**500**	**1000**	**5000**	**9000**
10	1.4 ± 7.8	1.4 ± 16.9	2.3 ± 16.8	3.7 ± 4.0	3.8 ± 3.5	4.1 ± 2.5
50	0.8 ± 44.7	2.6 ± 19.0	8.9 ± 3.5	8.7 ± 3.9	8.9 ± 1.9	9.3 ± 1.8
100	0.4 ± 44.7	4.7 ± 15.0	10.4 ± 2.1	11.0 ± 2.4	12.2 ± 1.7	13.5 ± 1.4
500	0.6 ± 29.8	5.8 ± 6.7	19.3 ± 1.2	19.5 ± 4.1	18.3 ± 1.1	21.5 ± 0.7
1000	0.6 ± 29.8	4.5 ± 12.7	18.9 ± 6.0	23.1 ± 2.6	20.5 ± 1.4	22.7 ± 0.5
5000	0.6 ± 44.7	4.2 ± 24.8	18.4 ± 2.1	22.5 ± 0.6	20.7 ±0.9	23.9 ± 0.8
10000	0.2 ± 44.7	4.5 ± 11.5	18.4 ± 4.1	21.3 ± 3.5	21.7 ± 0.6	23.2 ± 0.5
50000	2.2 ± 11.9	4.8 ± 21.1	20.6 ± 2.0	21.1 ± 2.7	20.7 ± 0.6	24.3 ± 0.8

3.3.2. Two point sources

For the two-point-sources measurement, Figure 19 shows that 1,000 iterations was sufficient to reach a quasi-stationary state for at least 500 counts. The data and uncertainties are also displayed in Table 7. This result confirmed that using 10,000 iterations for the two-point-sources neutron image was acceptable to reach the quasi-stationary state.

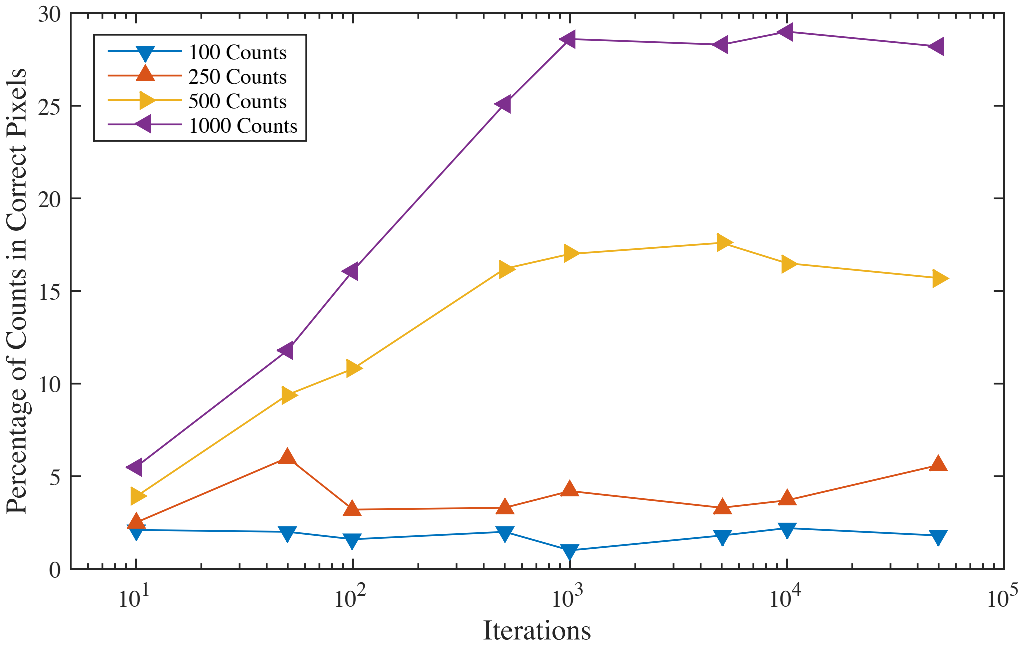

Figure 19: For two point sources, two parameters, total counts and number of iterations, were compared for differing numbers of counts. For cases with at least 500 counts, image quality did not improve after 1,000 counts.

Table 7: Percentage of neutron counts that reconstructed to the source pixels for different combinations of counts and iterations. The error is expressed as one standard deviation.

	Total Counts			
Iterations	**100**	**250**	**500**	**1000**
10	2.1 ± 9.1	2.5 ± 4.7	3.9 ± 4.6	5.5 ± 2.3
50	2.0 ± 6.7	6.0 ± 4.9	9.4 ± 3.2	11.8 ± 2.1
100	1.6 ± 6.0	3.2 ± 8.2	10.8 ± 5.5	16.1 ± 1.4
500	2.0 ± 9.4	3.3 ± 7.3	16.2 ± 2.7	25.1 ± 1.3
1000	1.0 ± 9.4	4.2 ± 5.7	17.0 ± 2.1	28.6 ± 1.0
5000	1.8 ± 9.7	3.3 ± 7.5	17.6 ± 2.1	28.3 ± 1.1
10000	2.2 ± 11.3	3.7 ± 5.4	16.5 ± 2.5	29.0 ± 0.7
50000	1.8 ± 16.9	5.6 ± 6.2	15.7 ± 2.1	28.2 ± 0.9

4. Conclusions

We showed that SOE image reconstruction can be applied to nuclear safeguards applications by presenting reconstructed images of measured and simulated sources. The algorithm proved effective for both neutron and photon imaging by demonstration of SOE imaging to discriminate between a point source, two point sources, and a distributed source. We also showed that SOE image reconstruction creates comparable images to an MLEM solution in terms of the percentage of counts reconstructing to the source regions.

Analysis of the angular resolution of the DPI showed that the majority of projected cones are within 8° of the actual source location, which implied that an 8° broadening for each projected cone allowed most origins to construct to the correct source location. The similar features found in the measured and simulated neutron distributions for the investigation of system resolution helped validate MCNPX-PoliMi and MPPost as a simulation tool for further investigation of the SOE method.

Results for the ^{252}Cf point source showed proper reconstruction for both the neutron and photon images. However, more noise was present in the photon image than in the neutron image. On average, the neutron image reconstructed 24.3% of the total counts to the correct source pixel while the photon image reconstructed only 2.1% of total counts to the correct source pixel. From these percentages, and examination of a simulated image, we concluded that the ratio of source-to-background-radiation was the cause of the noise in the photon images. The distributed-source photon image showed this effect with only about 1.0% of total counts located in each source pixel. When the percentage of photons in each source pixel is larger, such as it was for the two-point-source measurement (averages of 3.3% and 2.7%), a much lower contribution from noise was seen. Because rates of neutron background radiation are typically several orders of magnitude lower than that of photon radiation, there was very little noise in the reconstructed neutron images.

We also showed that there is a relationship between the total number of counts in a reconstruction, the number of iterations used, and image quality. For a point source, when at least 1,000 counts were used, increasing the number of iterations past 1,000 did not improve the image quality. However, when more counts were used, a higher percentage of the total reconstructed to the source pixel. For two point sources the results were similar and showed that increasing the number of iterations past 1,000 did not improve image quality and that more total counts used in the image reconstruction allowed a higher percentage to reconstruct to the source pixel.

Future work will investigate the combination of the neutron and photon data for SOE image reconstruction. A fusion of the measured neutron and photon results for the distributed source may allow for a more consistent reconstruction with a good signal-to-noise ratio. Investigations will also include further improvement to the algorithm to achieve better reconstruction with a low number of counts and smaller pixel sizes.

Acknowledgements

This work is supported in-part by the National Nuclear Security Administration through NA-22 funding opportunity DE-FOA-0000568. It is also funded in-part by the Consortium for Verification Technology under Department of Energy National Nuclear Security Administration award number DE-NA0002534. M.C. Hamel and J.K. Polack are funded in-part by the Sandia National Laboratories Excellence in Engineering Research Fellowship. The prototype system is funded in-part by the Department of Energy, Nuclear Energy University Program, award number DE-NE0000324.

5. References

[1] P. E. Vanier and L. Forman, "Demonstration of a directional fast neutron detector," in *IEEE Nuclear Science Symposium Conference Record*, 2005, vol. 1, pp. 116–119.

[2] N. Mascarenhas, J. Brennan, K. Krenz, P. Marleau, and S. Mrowka, "Results with the neutron scatter camera," in *IEEE Nuclear Science Symposium Conference Record*, 2008, vol. 56, no. 3, pp. 3368–3371.

[3] S. J. Wilderman, N. H. Clinthorne, J. A. Fessler, and W. L. Rogers, "List-mode maximum likelihood reconstruction of Compton scatter camera images in nuclear medicine," *1998 IEEE Nucl. Sci. Symp. Conf. Rec.*, vol. 3, pp. 1716–1720, 1998.

[4] C. Lehner, Z. He, and F. Zhang, "4π Compton Imaging Using a 3-D Position-Sensitive Maximum Likelihood," *IEEE Trans. Nucl. Sci.*, vol. 51, no. 4, pp. 1618–1624, 2004.

[5] J. W. Leblanc, N. H. Clinthorne, C. H. Hua, E. Nygard, W. L. Rogers, D. K. Wehe, P. Weilhammer, and S. J. Wilderman, "Experimental results from the C-SPRINT prototype compton camera," *IEEE Trans. Nucl. Sci.*, vol. 46, no. 3 PART 1, pp. 201–204, 1999.

[6] K. Vetter, M. Burks, and L. Mihailescu, "Gamma-ray imaging with position-sensitive HPGe detectors," *Nucl. Instruments Methods Phys. Res. Sect. A Accel. Spectrometers, Detect. Assoc. Equip.*, vol. 525, no. 1–2, pp. 322–327, 2004.

[7] A. Andreyev, A. Sitek, and A. Celler, "Fast image reconstruction for Compton camera using stochastic origin ensemble approach.," *Med. Phys.*, vol. 38, no. 1, pp. 429–438, 2011.

[8] A. Sitek, "Representation of photon limited data in emission tomography using origin ensembles.," *Phys. Med. Biol.*, vol. 53, no. 12, pp. 3201–3216, 2008.

[9] A. Andreyev, A. Sitek, and A. Celler, "Stochastic image reconstruction method for compton camera," *IEEE Nucl. Sci. Symp. Conf. Rec.*, pp. 2985–2988, 2009.

[10] D. Mackin, S. Peterson, S. Beddar, and J. Polf, "Evaluation of a stochastic reconstruction algorithm for use in Compton camera imaging and beam range verification from secondary gamma emission during proton therapy," *Phys. Med. Biol.*, vol. 57, no. 11, pp. 3537–3553, 2012.

[11] R. C. Runkle, "Neutron sensors and their role in nuclear nonproliferation," *Nucl. Instruments Methods Phys. Res. Sect. A Accel. Spectrometers, Detect. Assoc. Equip.*, vol. 652, no. 1, pp. 37–40, 2011.

[12] A. Poitrasson-Rivière, M. C. Hamel, J. K. Polack, M. Flaska, S. D. Clarke, and S. A. Pozzi, "Dual-particle imaging system based on simultaneous detection of photon and neutron collision events," *Nucl. Instruments Methods Phys. Res. Sect. A Accel. Spectrometers, Detect. Assoc. Equip.*, vol. 760, pp. 40–45, 2014.

[13] M. C. Hamel, A. Poitrasson-rivière, J. K. Polack, S. D. Clarke, M. Flaska, and S. A. Pozzi, "Design and Analysis of a Two-Plane Dual-Particle Imaging System," in *Proceedings of the INMM 54th Annual Meeting*, 2013.

[14] A. Andreyev, A. Celler, and A. Sitek, "Resolution recovery for compton camera using origin ensemble algorithm," *IEEE Nucl. Sci. Symp. Conf. Rec.*, pp. 2774–2778, 2012.

[15] A. Poitrasson-Rivière, J. K. Polack, M. C. Hamel, D. D. Klemm, K. Ito, A. T. McSpaden, M. Flaska, S. D. Clarke, S. A. Pozzi, A. Tomanin, and P. Peerani, "Angular-resolution and material-characterization measurements for a dual-particle imaging system with mixed-oxide fuel," *Nucl. Instruments Methods Phys. Res. Sect. A Accel. Spectrometers, Detect. Assoc. Equip.*, vol. 797, pp. 278–284, 2015.

[16] S. A. Pozzi, S. D. Clarke, W. J. Walsh, E. C. Miller, J. L. Dolan, M. Flaska, B. M. Wieger, A. Enqvist, E. Padovani, J. K. Mattingly, D. L. Chichester, and P. Peerani, "MCNPX-PoliMi for nuclear nonproliferation applications," *Nucl. Instruments Methods Phys. Res. Sect. A Accel. Spectrometers, Detect. Assoc. Equip.*, vol. 694, pp. 119–125, 2012.

[17] E. C. Miller, S. D. Clarke, M. Flaska, S. Prasad, S. A. Pozzi, and E. Padovani, "MCNPX-PoliMi Post-processing Algorithm for Detector REsponse Simulations," *J. Nucl. Mater. Manag.*, vol. XL, no. 2, pp. 34–41, 2012.

[18] A. Enqvist, C. C. Lawrence, B. M. Wieger, S. A. Pozzi, and T. N. Massey, "Neutron light output response and resolution functions in EJ-309 liquid scintillation detectors," *Nucl. Instruments Methods Phys. Res. Sect. A Accel. Spectrometers, Detect. Assoc. Equip.*, vol. 715, pp. 79–86, 2013.

[19] K. Roemer, G. Pausch, C. M. Herbach, M. Kapusta, Y. Kong, R. Lentering, C. Plettner, J. Stein, M. Moszynski, Ł. Swiderski, and T. Szczęśnik, "Energy resolution and nonlinearity of NaI(Tl), CaF2(Eu), and plastic scintillators measured with the wide-angle Compton-coincidence technique," *IEEE Nucl. Sci. Symp. Conf. Rec.*, vol. 2, pp. 580–586, 2010.

[20] J. K. Polack, A. Poitrasson-Riviere, M. C. Hamel, M. F. Becchetti, K. Ide, S. D. Clarke, M. Flaska, and S. A. Pozzi, "Image reconstruction using a three-plane, dual-particle imager for standoff detection of special nuclear material," in *IEEE Nuclear Science Symposium Conference Record*, 2012, pp. 118–121.

[21] J. K. Polack, M. C. Hamel, P. Marleau, M. Flaska, S. D. Clarke, and S. A. Pozzi, "Spectrum Isolation in Multi-Source Image Reconstruction Using a Dual-Particle Imager," in *Proceedings of the INMM 56th Annual Meeting*, 2015.